J. Fluid Mech. (1990), *vol.* 221, *pp.* 77–103
Printed in Great Britain

Thermocapillary convection in long horizontal layers of low-Prandtl-number melts subject to a horizontal temperature gradient

By HAMDA BEN HADID AND BERNARD ROUX
Institut de Mécanique des Fluides, UM 34 du CNRS, 1 Rue Honnorat, F-13003 Marseille, France

(Received 2 February 1988 and in revised form 3 May 1990)

Thermocapillary convection arising in small-depth layers (long horizontal cavities) subject to a horizontal temperature gradient is studied numerically. A broad range of values of the Reynolds–Marangoni number, Re, is considered for three values of the aspect ratio (A = length/height). For the largest aspect ratio considered, $A = 25$, the fully developed Poiseuille–Couette solution is reached, but only for moderate Re. The limiting Re value for the observability of such a fully developed solution is derived as a function of $A (Re \leqslant 20A)$. For $Re \leqslant 20A$, the flow exhibits three distinct regimes, in the upwind, central and downwind regions, respectively. The Poiseuille–Couette solution (when it exists) fills the central region, and the flow is accelerated, in the upwind region, to reach this Poiseuille–Couette solution at a distance that is proportional to Re. In the downwind region, where the flow is deflected by the endwall, a multi-roll structure is exhibited for $Re \geqslant 1330$. The number of rolls increases with Re. When $Re > 20A$, the upwind and downwind regions coalesce and some of the downwind rolls can be suppressed. Most of the computations concern interfacial conditions (with fixed temperature distribution) for which the dynamical solution is decoupled from the thermal one. A few thermal solutions are given herein, for $Pr = 0.015$ only.

1. Introduction

This study is devoted to horizontal layers of fluids at low Prandtl number, Pr, in a long rectangular cavity whose vertical endwalls are maintained at different temperatures. Our main motivation is to study the velocity field prevailing during the growth, from their melts, of metal and semiconductor crystals (such as GaAs) in long horizontal open boats (e.g. by the Bridgman technique). We consider situations in which the depth of the melt is small enough to ensure the dominance of the thermocapillary forces over the buoyancy forces. The necessary conditions for this dominance can be estimated through the previous works reviewed by Ostrach (1982) and the results given by Napolitano (1982) by an order of magnitude analysis.

Numerous studies have been devoted to the onset of Marangoni convection in long horizontal layers but subject to a vertical temperature gradient (even in the case of coupling with buoyancy convection). These studies include experimental, theoretical (stability) and numerical approaches. Among these are Pearson (1958), Nield (1964), Scriven & Sterling (1964), Smith (1966), Ostrach (19760, Castillo & Velarde (1982), Cerisier *et al.* (192), Sen & Davis (1982), Platten & Legros (1986), Velarde, Garcia-Ybarra & Castillo (1987), Winters, Plesser & Cliffe (1988) and Benguria & Depassier (1989).

Several papers address the problem of steady and oscillatory convection in liquid columns with free cylindrical surfaces as they occur in the floating zones technique, especially for the case of a microgravity environment (see e.g. Chun 1980; Schwabe & Scharmann 1981, 1988; Cowley & Davis 1983; Preisser, Schwabe & Scharmann 1983; Fu & Ostrach 1983; Xu & Davis 1984; Napolitano & Monti 1987, and Kazarinoff & Wilkowski 1989). Thermocapillary convection also plays an important role in the Czochralski technique, as shown by Balasubramaniam & Ostrach (1984). For the problems of surface-tension-driven convection in connection with materials processing, the reviews by Carruthers (1977), Rosenberger (1979), Pimputkar & Ostrach (1981), Polezhaev (1984), Avduyevsky *et al.* (1984) and Langlois (1985) are relevant.

For open-boat systems, there are several ways in which a free liquid–gas interface can modify the convection in the bulk, depending on whether the interface is allowed to be deformed or remain flat, and whether or not it is subject to stresses induced by surface-tension gradients. Strictly speaking, when a liquid layer is subject to volume or surface convection, interfaces with the surrounding gas cannot be planar; this was demonstrated by Yih (1968). Several works have been devoted to deformed liquid–gas interfaces; see Pimputkar & Ostrach (1981), Sen & Davis (1982), Strani, Piva & Graziani (1983), Cuvelier & Driessen (1986), for instance. Nevertheless, the assumption of a planar liquid–gas interface is still often used; it seems appropriate for metallic melts as the capillary number is generally small in this case.

In the case of thermocapillary convection in layers with large horizontal extent and with small horizontal (constant) temperature gradients, G_h, the flow far from the vertical endwalls can be expected to be plane parallel (Poiseuille–Couette flow solution) as shown by Birikh (1966); in this case the relevant parameter is the Reynolds–Marangoni number, $Re = -(\partial\sigma/\partial T)\, G_h H^2/(\rho\nu^2)$. Experiments in parallelepiped cavities with such large horizontal dimensions have been done by Kirdyashkin (1984). He found that for long cavities (length = 412 mm; height = 9.4 mm) filled with ethyl alcohol ($4.5 \leqslant Pr \leqslant 5.5$) and for high Marangoni numbers ($Ma \approx 1.1 \times 10^4$, i.e. $Re = Ma/Pr \approx 2 \times 10^3$), the flow largely exhibits a plane-parallel pattern, for $120 \text{ mm} \leqslant y \leqslant 300 \text{ mm}$.

By applying linear stability theory to the basic Poiseuille–Couette-flow solution (given below by expression (9)) and taking a fixed heat flux (defined by the Biot number, Bi) as thermal boundary conditions along the horizontal surfaces, Smith & Davis (1983) found oscillatory instabilities that take the form of two hydrothermal waves (with angles $+\Phi$ and $-\Phi$ with respect to the negative y-axis) propagating obliquely to the direction of the surface flow. For low Pr, the mechanism for instability involves a transfer of energy from the horizontal temperature gradients of the basic state to the perturbations, through horizontal convection. In particular, Smith & Davis give neutral stability curves for the insulating case ($Bi = 0$). They also state that an increase in Bi always results in a more stable system; thus $Bi = 0$ minimizes the critical Marangoni number, Ma_c, for the onset of unsteady flow. For $Pr = 10^{-3}$, Ma_c is close to 2, and behaves as $Pr^{\frac{1}{2}}$ when Pr goes to zero; thus the critical value of Re increases as $Pr^{-\frac{1}{2}}$ when $Pr \rightarrow 0$. For $Pr = 0.015$ (where $Ma_c = 9$; i.e. $Re_c = 600$), Φ is close to 77°; this corresponds to an instability in the form of nearly longitudinal rolls (with axes nearly aligned in the direction of G_h). At the threshold the wavelength, λ_c, is close to $19H$ and the frequency (non dimensionalized by ν/H^2) is close to 2.4. Such instabilities can only be observed in large-width cavities. Note that this minimum width increases as $Pr \rightarrow 0$. For a recent review of thermocapillary instabilities see Davis (1987) and Smith (1988).

An asymptotic theory (for $A \to \infty$) has been developed by Sen & Davis (1982) and by Strani *et al.* (1983). In addition, Strani *et al.* (1983) performed numerical simulations and derived aspect-ratio conditions to get parallel flow in the core of the cavity ($A \geqslant 4$). The nonlinear effects which tend to destroy this parallel flow have been found to reach a contribution exceeding 10% for $Re > 100$.

A specific case where the surface tension presents an extremum with the temperature has been studied by Legros, Petré & Limbourg-Fontaine (1983) and Villers & Platten (1987) for aqueous solutions (Pr close to 7) in long horizontal cavities ($2 \leqslant A \leqslant 10$).

Thermocapillary and buoyancy convection in a rectangular container have been investigated for silicone oil ($Pr = 9200$) by Ochiai *et al.* (1984) who performed experiments for moderate Ma ($Ma \leqslant 50$) and for aspect ratios of order one ($0.5 \leqslant A \leqslant 2$). For small buoyancy forces (typically $Ra < 100$), the dominant thermocapillary forces lead to a flow pattern which is quite symmetric with respect to the vertical midplane ($y = \frac{1}{2}A$). This is probably because the Reynolds–Marangoni number Re is very small ($Re \approx 0.005$); the flow structure is quite simple and therefore well predicted by numerical simulation.

For intermediate Pr, namely $Pr = 1$, Polezhaev *et al.* (1981) studied the 'radial' segregation induced by the thermocapillary convection in rectangular cavities of moderate aspect ratio ($A = 1$ and $A = 2$). They obtained a one-cell solution for $Ma = 10^2$, 10^3 and 10^4. Napolitano, Golia & Viviani (1984) considered the transient thermocapillary convection in small-aspect-ratio cavities ($A = 0.25$ and $A = 1$) for $Re' = 1000$ (note that $Re' = A^{-2} Re$), for which the (vertical) deep-layer approximation applies for the steady state; the surface velocity is essentially constant in the central part of the cavity (60% of its length).

Concerning low-Pr fluids, some computations have been done for a square cavity ($A = 1$) by Wilke & Löser (1983) for Si melts ($Pr = 0.026$) at $Ma = 7 \times 10^2$ and $Ma = 7 \times 10^3$ ($Re = 2.7 \times 10^4$ and $Re = 2.7 \times 10^5$ respectively), in the case of non-constant driving forces (sinusoidal temperature distribution) on the upper surface; steady solutions were obtained with a one-cell and a three-cell structure, respectively, for these two Ma values. Srinivasan & Basu (1986) also considered a sinusoidal temperature distribution for laser melting of iron, performing computations for $Pr = 0.1$, $0.2 \leqslant A \leqslant 5$ and $4 \times 10^2 \leqslant Re \leqslant 10^4$. For square cavities ($A = 1$), the maximum horizontal velocity increases linearly with Re for $Re < 10^3$, and as $Re^{\frac{2}{3}}$ for $Re > 5 \times 10^3$. For cavities subject to a monotonic horizontal temperature gradient, only a few results are available at present (see numerical studies by Zebib, Homsy & Meiburg (1985) for square cavities, Bergman & Keller (1988) for moderate aspect ratios ($0.5 \leqslant A \leqslant 2$), and Ben Hadid *et al.* (1987) and Villers & Platten (1989) for $A = 4$). Measurements of the surface velocity, performed for liquid tin ($Pr = 0.015$) by Camel, Tison & Favier (1986), show a linear increase of the velocity with Re in the range $0 < Re < 10^3$; while at higher Re the velocity increases less rapidly than linearly.

Experimental visualization of the structure of the shear-driven isothermal flow in an open cavity of $A = 3.5$ by Neary & Stephanoff (1987) shows that a single vortex with a diameter approximately equal to the depth of the cavity develops downstream of the geometric centre of the cavity. As the Reynolds number rises owing to an increase of the external (free stream) velocity, two supplementary vortices appear; a counter-rotating vortex due to the flow separation forms close to the bottom wall and a corotating one appears upstream of the primary vortex. This visualization is

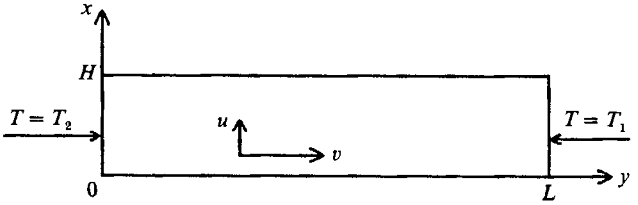

FIGURE 1. The two-dimensional model of an open rectangular cavity.

for water ($Pr \approx 7$). Visualizations of the flow structure for low-Prandtl-number fluids are not known to the authors.

The aim of the present paper is to fill a gap by analysing the two-dimensional thermocapillary convection in an open rectangular cavity for $A = 4$, $A = 12.5$ and $A = 25$. The upper surface of the fluid, which is subject to a shear due to the change in surface tension, is assumed to remain flat. We assume no buoyancy ($g = 0$, or $Gr = 0$) in order to uncouple the buoyancy and thermocapillary effects. In addition, in most of the computations we consider a linear temperature distribution along the free surface. In that case, with constant $\partial T/\partial y$ and constant $\partial \sigma/\partial T$, the flow is driven by a prescribed stress, and the dynamic and thermal fields become uncoupled. We shall mainly consider the dynamical problem which is similar to the one studied by Bye (1966) who also emphasized the stability analysis of the Poiseuille–Couette (mid-basin) solution with respect to 'upwind' and 'downwind' disturbances. In the following, we shall adopt this terminology, in which the upwind region is closer to the hot wall, and the downward region is closer to the cold endwall (for a 'normal' thermocapillary effect, i.e. when $\partial \sigma/\partial T < 0$).

The assumption of fixed temperature distribution along the free surface is reasonable only for small Pr and small Re. The time-dependent two-dimensional Navier–Stokes equations are numerically solved by using a finite-difference technique. The energy equation (which is uncoupled in most of the applications considered herein) is only computated for $Pr = 0.015$. The work presented herein is a part of a much broader study devoted to metallic melts, made in the framework of the Doctorate Thesis by Ben Hadid (1989).

2. Formulation of the problem

We consider an open rectangular cavity, of height H and length L (with aspect ratio $A = L/H$ greater than unity), having two differentially heated vertical endwalls at temperatures T_1 and T_2, with $T_2 > T_1$ (see figure 1), and filled with a fluid of low Prandtl number, $Pr = \nu/\kappa$, where ν and κ are respectively the kinematic viscosity and thermal diffusivity. As soon as $\Delta T = T_2 - T_1$ differs from zero, a thermocapillary-driven flow is generated owing to the temperature-induced change in the surface tension, σ, along the upper horizontal surface. The flow strength is characterized by the Reynolds–Marangoni number defined as $Re = -(\partial \sigma/\partial T)\, G_h H^2/(\rho \nu^2)$, where ρ is the density and $G_h = \Delta T/L$. Sometimes, we shall also use the Marangoni number defined as $Ma = Pr\, Re$.

2.1. *Two-dimensional governing equations*

The velocity is assumed to be small enough to consider the flow as laminar. In addition, the fluid is assumed to be Newtonian and incompressible. We shall consider the continuity and Navier–Stokes equations with the stream function and vorticity

(ψ and Ω) formulation; and we shall take $t_{\text{ref}} = H^2/\nu$ and $v_{\text{ref}} = (\nu/H)\,Re$ as time and velocity scales. So, we have $\psi_{\text{ref}} = \nu Re$ and $\Omega_{\text{ref}} = (\nu/H^2)\,Re$ as stream-function and vorticity references.

Thus, the governing equations can be written as

$$\Omega_t + Re(u\Omega_x + v\Omega_y) = (\Omega_{xx} + \Omega_{yy}), \tag{1}$$

$$\psi_{xx} + \psi_{yy} + \Omega = 0, \tag{2}$$

with

$$u = \psi_y, \quad v = -\psi_x, \quad \Omega = v_x - u_y. \tag{3}$$

The energy transport equation is then

$$\theta_t + Re(u\theta_x + v\theta_y) = Pr^{-1}\,(\theta_{xx} + \theta_{yy}),$$

where

$$\theta = (T - T_1)/T_{\text{ref}}, \quad \text{with } T_{\text{ref}} = \Delta T/A. \tag{4}$$

2.2. *Boundary conditions*

(i) On the rigid walls ($x = 0$, $y = 0$, $y = A$):

$$u = v = 0; \tag{5}$$

(ii) on the upper boundary ($x = 1$) which is assumed to be flat we have

$$u = 0,$$

and according to Birikh (1966), the equilibrium condition is

$$\partial v/\partial x = -\partial\theta/\partial y \tag{6}$$

(iii) on the isothermal vertical walls we have

$$\theta_{(x,0)} = \theta_2 = A; \quad \theta_{(x,A)} = \theta_1 = 0, \tag{7}$$

(iv) while on the horizontal boundaries we consider two kinds of thermal conditions; either

$$\theta_x = 0 \qquad \text{(insulating)} \tag{8a}$$

or

$$\theta = A - y \qquad \text{(`perfectly conducting')}. \tag{8b}$$

We can recall that in the case (8*b*) we have a pure fluid flow problem, because the flow is driven by a prescribed stress (6), as $\partial v/\partial x$ is constant.

2.3. *Infinitely long cavity, $A \rightarrow \infty$ (Birikh solution)*

For the case of an infinitely long cavity (finite H and infinite L), a steady one-dimensional flow solution exists for low Re, such that $u = 0$ and $v = v(x)$.

Accounting for the mass flux conservation in a vertical plane ($\int_0^1 v\,dx = 0$) and the conditions (5) and (6), the Poiseuille–Couette solution applies for the longitudinal velocity (see Birikh, 1966):

$$v_{\text{PC}}(x) = \tfrac{1}{4}(3x - 2)\,x. \tag{9}$$

A vertical temperature profile, $T(x)$, can be associated with $v(x)$, such that $\theta(x,y) = T(x) + (A - y)$; $T(x)$ is derived from (4) and (9), by integrating

$$T_{xx} = \theta_{xx} = Pr\,Re\,v\theta_y = -\tfrac{1}{4}Ma\,[3x^2 - 2x].$$

So, for insulating horizontal surfaces, the condition (8*a*) can be written as

$$T_{\text{PC}}(x) = -\tfrac{1}{48}Ma\,(3x^4 - 4x^3 + 0.4); \tag{10a}$$

while, for conducting horizontal surfaces, the condition (8*b*) becomes

$$T_{\text{PC}}(x) = -\tfrac{1}{48}Ma\,(3x^4 - 4x^3 + x). \tag{10b}$$

Grid meshes	31 × 161		35 × 201		37 × 251	
$Re \times 10^{-3}$	ψ_{max}	$(v_{surf})_{max}$	ψ_{max}	$(v_{surf})_{max}$	ψ_{max}	$(v_{surf})_{max}$
3.333	0.05156	0.2556	0.05153	0.2557	0.05153	0.2548
5.0	0.04700	0.2375	0.04741	0.2364	0.04729	0.2347
6.667	0.04329	0.2227	0.04403	0.2210	0.04383	0.2189

TABLE 1. Characteristic flow results for $A = 25$

Expressions 10a, b) show that the temperature variation in the vertical direction (and thus the temperature stratification in this direction, $\partial\theta/\partial x$) is proportional to Ma.

3. Numerical finite-difference method

The derivation of the discretized two-dimensional equations is not given here but it follows the approach described elsewhere (Roux *et al.* 1978; Ben Hadid 1989). The numerical technique used to solve the system (1)–(8) is an extension to purely unsteady equations of the pseudo-unsteady algorithm described in detail in the two papers cited above and used to improve the rate of convergence of the iterative process induced by the nonlinearity and the coupling of the governing equations. The main features of this numerical technique are:

(i) an alternating direction implicit (ADI) method for solving the finite difference equations (1), (2) and (4),

(ii) a second-order central differentiation for spatial derivatives for (1) and (4),

(iii) a fourth-order compact Hermitian method for (2), and

(iv) internal iterations to adjust the values of ψ at every iteration.

The block-tridiagonal matrix inversion algorithm (Thomas algorithm), resulting from the use of high order Hermitian finite-difference relationships, was employed for (2). The vorticity at the boundary was calculated with the third-order relationship (known in the literature as Hirsh's relationship) and already used for natural convection problems by Roux *et al.* (1979). We included a compatibility condition for variables on boundaries at the intermediate time level (Fairweather & Mitchell 1967); and an iterative process at each time step. The convergence criterion was based on the vorticity variation at the boundary. A solution of the Navier–Stokes equations is considered to be converged when the variation of the (reduced) vorticity at the boundary is less than 0.01%.

The grid size effect has been controlled for the largest cavity, $A = 25$, by comparing the results obtained with three different non-uniform grids (with 31 × 161, 35 × 201 and 37 × 251 points, respectively). Details about the grid influence on the main characteristics of the flow (maximum of the stream function, ψ_{max}, and maximum of the surface velocity, $(v_{surf})_{max}$) are given in table 1.

Table 1 shows that, for $Re = 6.667 \times 10^3$, the maximum variations of ψ_{max} and $(v_{surf})_{max}$ with respect to the grid change are less than 1.5% and 2% respectively. Thus, a satisfactory accuracy can be reached with the intermediate grid (i.e. with 35 × 201 points), in the case of $A = 25$. The majority of the solutions reported in the present paper correspond to a non-uniform grid with 31 × 91 points for $A = 4$, 31 × 161 points for $A = 12.5$, and 35 × 201 points for $A = 25$. A non-uniform grid is needed not only for the usual grid refinement near the boundaries (rigid walls, or

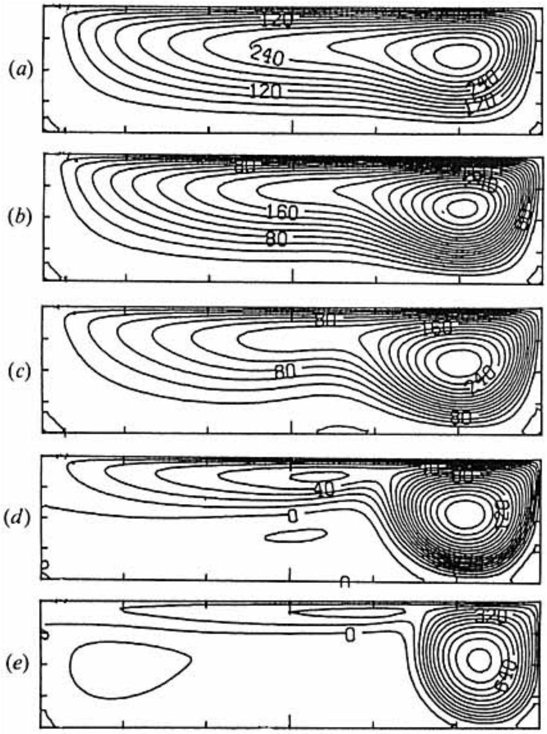

FIGURE 2. Streamline patterns in the conducting case for various Reynolds–Marangoni numbers. (*a*) Re = 3.33×10^2; (*b*) 6.67×10^2; (*c*) 1.33×10^3; (*d*) 6.67×10^3; (*e*) 3.33×10^4. $A = 4$.

upper free-surface subject to shear stress), but also to account for the non-symmetry of the flow (between upwind and downwind regions). The finest grid size, which is used near the downwind endwall, is about three times smaller than the one corresponding to a uniform grid. The grid size is gradually increased away from the boundaries. The numerical experiments were performed for various values of the time step, which depends on the number of grid points, the local refinement close the sidewalls and the value of the Reynolds number. As a rule the time step is decreased when Reynolds number is increased. The majority of the solutions reported in this paper are obtained with a time step ranging from 1×10^{-4} to 5×10^{-4}.

4. Results and discussion

We have considered thermocapillary convection for both insulating and conducting thermal boundary conditions on the horizontal surfaces. Computations are performed for three values of the aspect ratio ($A = 4$, $A = 12.5$ and $A = 25$) and for a wide range of Reynolds–Marangoni numbers ($1 \leqslant Re \leqslant 5 \times 10^4$), where the lowest Re considered is below the threshold value obtained from the stability results of Smith & Davis (1983).

4.1. *Conducting horizontal surfaces* (*at* $A = 4$)

The flow structure evolution can be seen in figure 2 for five selected values of Re (3.33×10^2; 6.67×10^2; 1.33×10^3; 6.67×10^3 and 3.33×10^4). At lower Re, a concentrated vortex forms near the cold wall, the strength of which increases with Re. Above $Re = 1.33 \times 10^3$, a counter-rotating cell occurs in the lower part of the layer

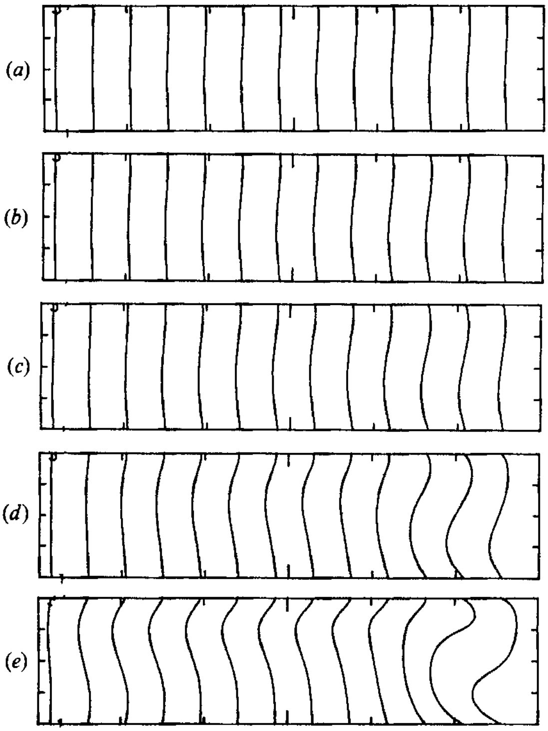

FIGURE 3. Isotherm patterns in the conducting case for various Reynolds–Marangoni numbers. (*a*) $Re = 3.33 \times 10^2$; (*b*) 6.67×10^2; (*c*) 1.33×10^3; (*d*) 6.67×10^3; (*e*) 3.33×10^4. $A = 4$.

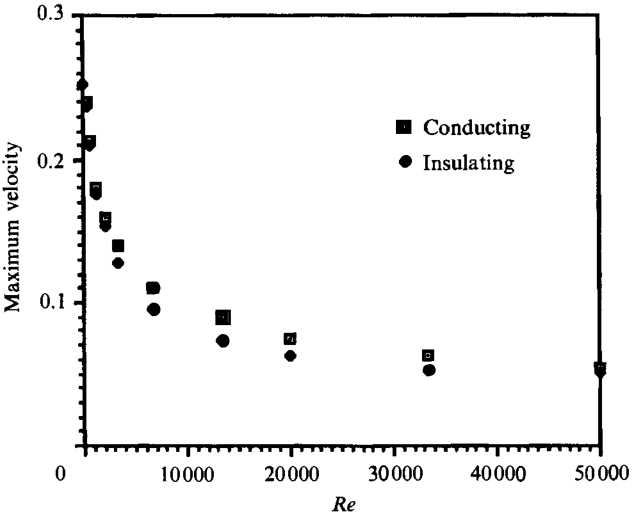

FIGURE 4. Maximum of the horizontal velocity component $v_{\max}$ *vs*. Re; for conducting and insulating cases. $A = 4$.

and eventually moves to the hot endwall. The strength of this secondary flow also increases with Re. The corresponding isotherm patterns are shown in figure 3; these isotherms appear to be only slightly affected by the bulk flow, except for the highest Re value ($Re = 3.33 \times 10^4$) in the region of the strong primary vortex near the cold wall.

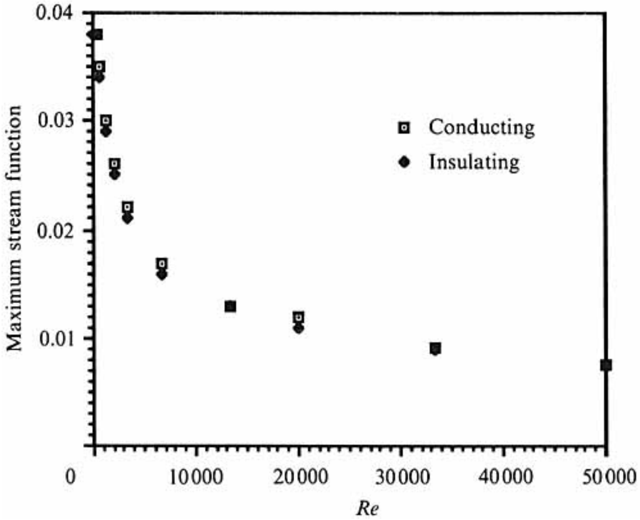

FIGURE 5. Maximum of the stream function Ψ_{max} *vs.* *Re*; for conducting and insulating cases. $A = 4$.

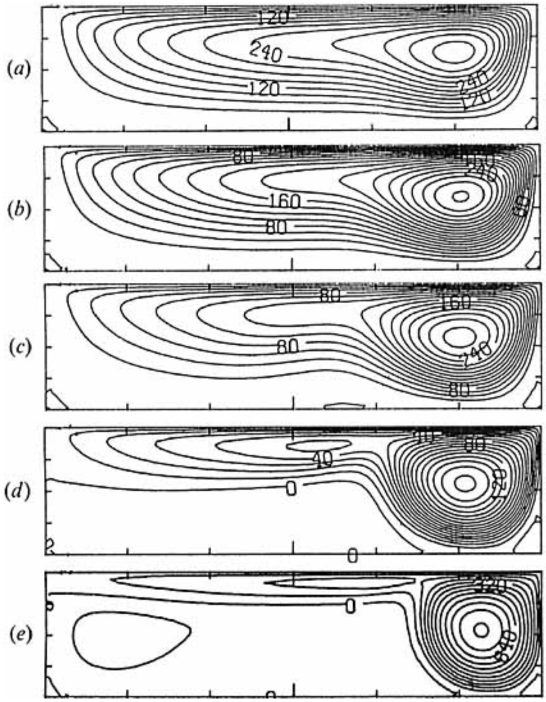

FIGURE 6. Streamline patterns in the insulating case for various Reynolds–Marangoni numbers. (*a*) $Re = 3.33\times10^2$; (*b*) 6.67×10^2; (*c*) 1.33×10^3; (*d*) 6.67×10^3; (*e*) 3.33×10^4. $A = 4$.

The evolution of Ψ_{max} and v_{max} is plotted in figures 4 and 5 in terms of *Re*; an asymptotic behaviour is found for high *Re*.

The computed flow structure can be compared to the experimental results obtained by Neary & Stephanoff (1987) for a shear-driven isothermal flow in an open cavity of $A = 3.5$ and for a Reynolds number, based on the leading-edge distance, of

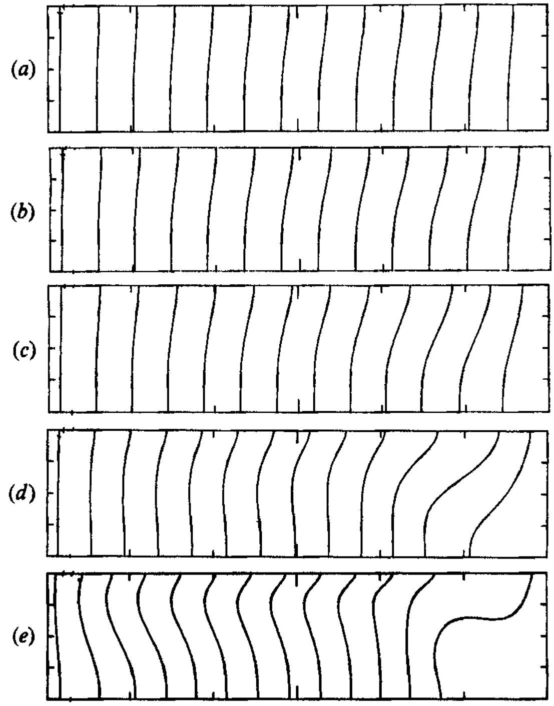

FIGURE 7. Isotherm patterns in the insulating case for various Reynolds–Marangoni numbers. (a) $Re = 3.33\times10^2$; (b) 6.67×10^2; (c) 1.33×10^3; (d) 6.67×10^3; (e) 3.33×10^4. $A = 4$.

11300 (see their figure 3), which is equal to $Re = 3630$ with our definition. Their observations, which are obtained for water ($Pr \approx 7$), agree qualitatively with the stable multicell structure we have found for $A = 4$, and for $Re = 1.33\times10^3$ and $Re = 6.67\times10^3$ (see figures 2(c) and 2(d), respectively. But one must be cautious about such comparisons, because of the difference in the value of the Prandtl number between metallic liquid and the transparent fluid (water) used in the experiment. Indeed, the coupling between flow and heat transfer is stronger for high Prandtl number and would significantly influence the flow structure for large Re. This remark is also well supported by the numerical calculations of Zebib *et al.* (1985) which show that the Prandtl number has a rather significant effect on the flow structure in a square cavity; the centre of the single vortex located in front of the vertical isothermal cold wall for Prandtl number equal to 0.001 is in front of the hot isothermal vertical wall when the Prandtl number is set equal to 50.

4.2. *Insulating horizontal surfaces* (*at* $A = 4$)

For insulating horizontal boundaries, the flow patterns shown in figure 6 are quite similar to the one presented in figure 2 for conducting boundaries. Similarly, the isotherm patterns in figure 7 present only small differences with respect to those in figure 3, except near the cold wall, in the region of the strong vortex. The evolution of $\Psi_{\max}$ and $v_{\max}$, again plotted in figures 4 and 5 as a function of Re, also present an asymptotic behaviour, as for the conducting case. One sees that the specific nature of the horizontal boundaries, conducting or insulating, does not play an important role in the range $Re < 5\times10^4$.

In figure 8 we compare the numerical v-velocity profile across the layer at $y = \frac{1}{2}A$ with the analytical solution given by (9) for infinitely large A. For $Re = 66.7$, figure

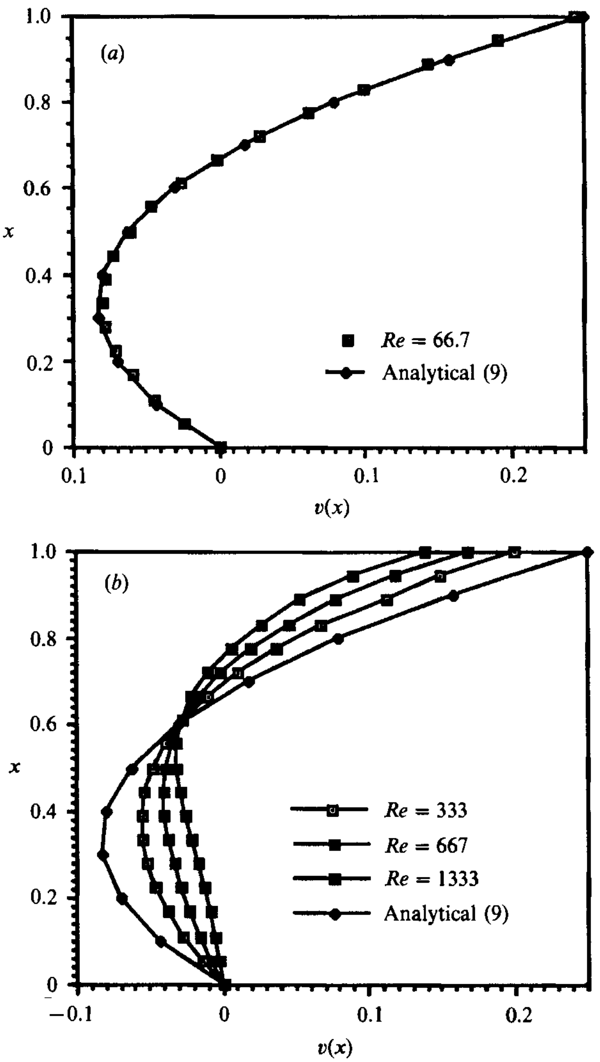

FIGURE 8. Vertical profile of the horizontal velocity component $v(x)$ at $y = \frac{1}{2}A$ for $A = 4$: (*a*) $Re = 66.7$, (*b*) $Re > 66.7$.

8(*a*) shows an excellent agreement with the non-dimensional analytical profile (9) which is independent of *Ma* and *Pr* (but we recall that the reference velocity is proportional to $Re = Ma/Pr$). In figure 8(*b*) we can see that the v-profile, at $y = \frac{1}{2}A$, rapidly differs from the analytical one when *Re* is increased. In addition, the value of v at $x = 1$ differs increasingly from the analytical value 0.25. The evolution of the velocity at the surface ($x = 1$) along the y-direction is presented in figure 9, in the interval $0.5 \leqslant y/A \leqslant 1$, with increasing *Re*. The curves shows a maximum closer to the cold endwall, the (non-dimensionalized) value of which decreases because of an increasing endwall effect (near the cold wall). One can also see that the surface velocity does not reach the asymptotic value of 0.25. The v-profiles for $Re = 1.33 \times 10^3$ at $y/A = 0.5$ and $y/A = 0.85$ are compared in figure 10 to the analytical one; the flow pattern, for moderate A, differs rapidly from the analytical one and becomes strongly y-dependent.

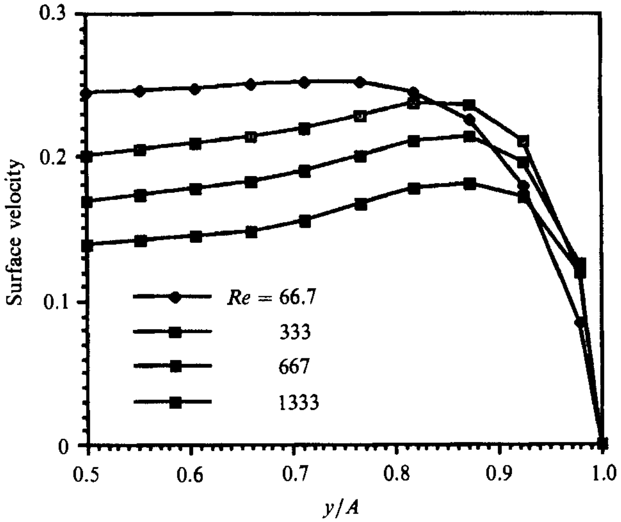

FIGURE 9. Surface velocity *vs.* y/A for $0.5 \leqslant y/A \leqslant 1$ at $A = 4$.

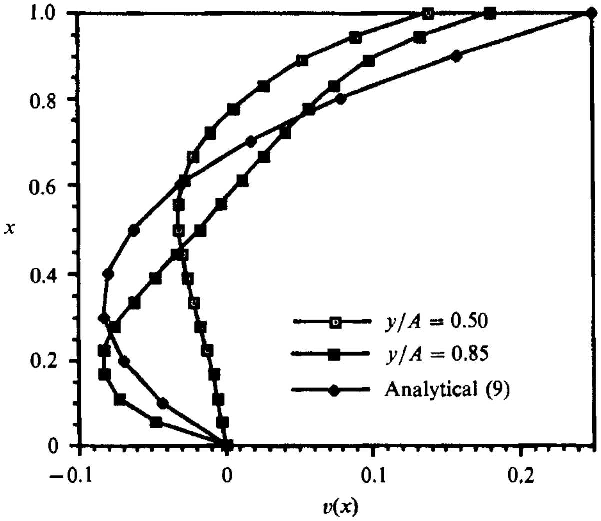

FIGURE 10. Vertical profile of the horizontal velocity component $v(x)$ at $y/A = 0.5$ and $y/A = 0.85$; for $A = 4$ and $Re = 1.33 \times 10^3$.

Summarizing, we see that for small Re ($Re \approx 67$) the flow pattern presents three regions: a central one which corresponds to a fully developed Poiseuille–Couette flow, an upwind one in which the flow is accelerated to reach this Poiseuille–Couette solution and a downwind region in which the flow is decelerated and stopped by the endwall at $y = A$. When Re increases, the length of the region of fully developed Poiseuille–Couette flow is reduced and eventually disappears, and then the upwind and downwind regions coalesce.

4.3. *Conducting horizontal surfaces* (*at higher* A)

We also performed computations for higher values of the aspect ratio (namely $A = 12.5$ and $A = 25$). Because of the similarity found in §4.2. for the two different types

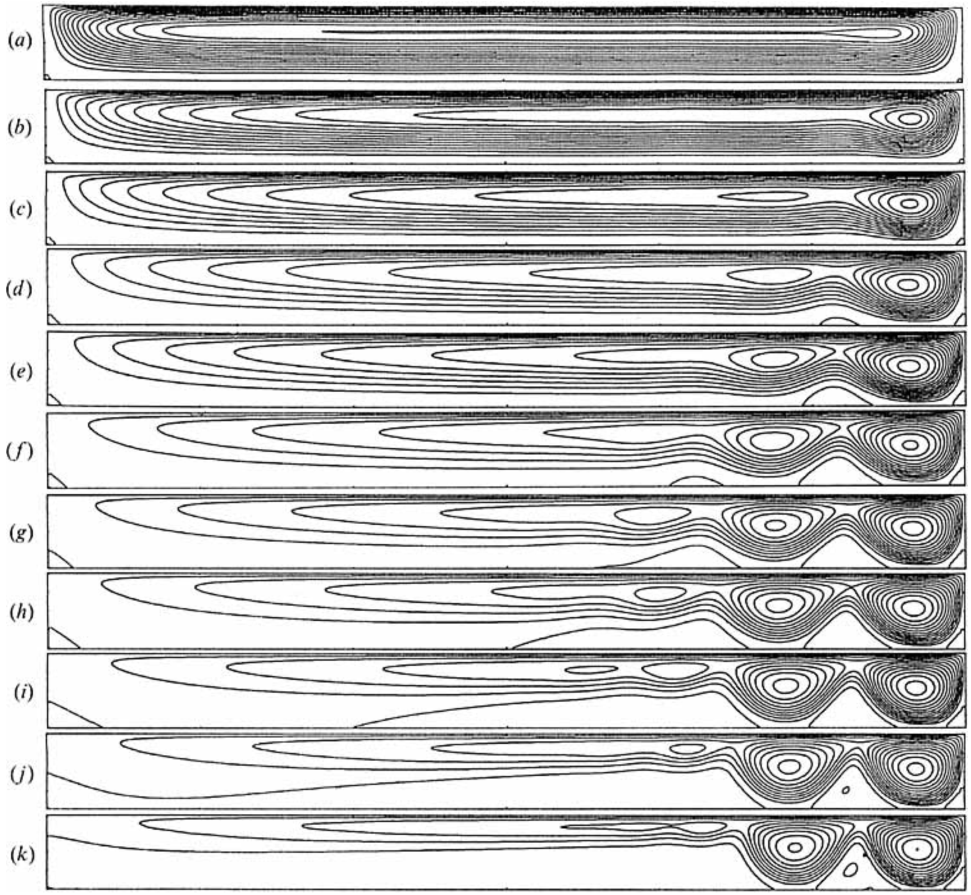

FIGURE 11. Streamline patterns in the conducting case for various *Re* at $A = 12.5$. (*a*) $Re = 66.7$; (*b*) 3.33×10^2; (*c*) 6.67×10^2; (*d*) 1.33×10^3; (*e*) 2×10^3; (*f*) 3.33×10^3; (*g*) 5×10^3; (*h*) 6.67×10^3; (*i*) 1×10^4; (*j*) 1.33×10^4; (*k*) 2×10^4.

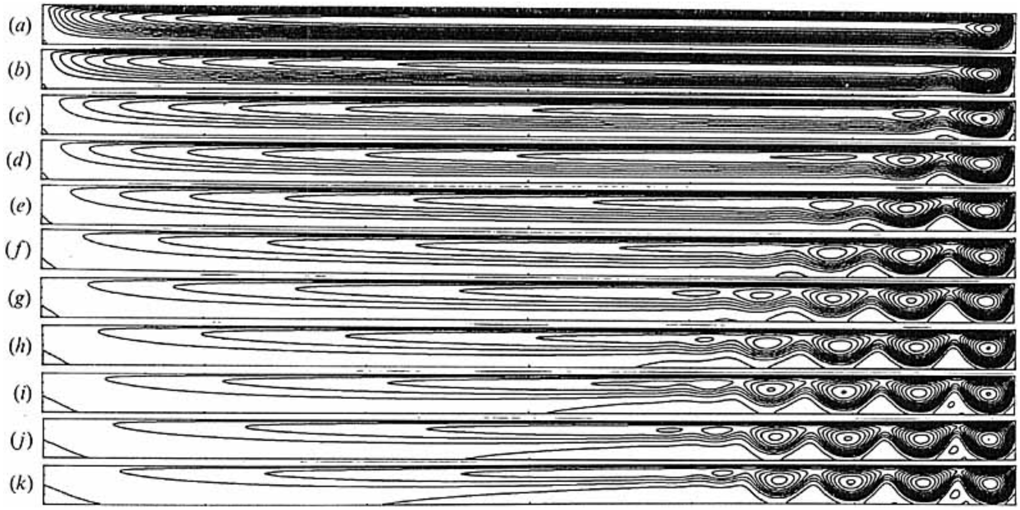

FIGURE 12. Streamline patterns in the conducting case for various *Re* at $A = 25$. (*a*) $Re = 66.7$; (*b*) 3.33×10^2; (*c*) 6.67×10^2; (*d*) 1.33×10^3; (*e*) 2×10^3; (*f*) 3.33×10^3; (*g*) 5×10^3; (*h*) 6.67×10^3; (*i*) 1×10^4; (*j*) 1.33×10^4; (*k*) 1.67×10^4.

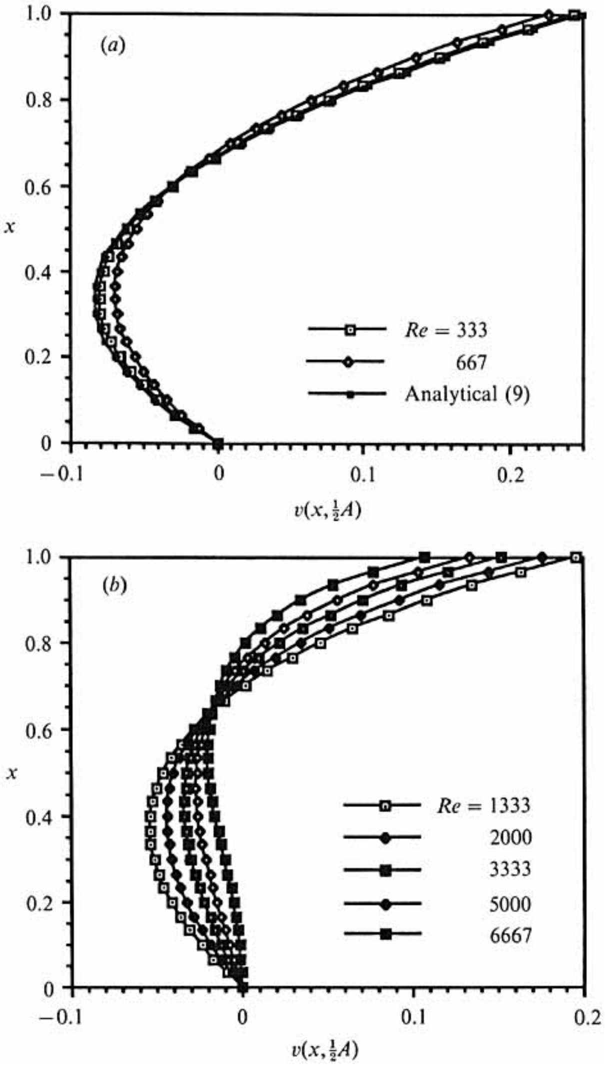

FIGURE 13. Velocity profile $v(x)$ at $y = \frac{1}{2}A$ for $A = 12.5$: (*a*) $Re \leqslant 6.67 \times 10^2$; (*b*) $Re \geqslant 1.33 \times 10^3$.

of thermal boundary conditions, we considered here only the conducting case for which the velocity and temperature fields are completely uncoupled.

The flow patterns for several values of Re and for $A = 12.5$ and $A = 25$ are given in figures 11 and 12, respectively. For small Re the flow patterns again present three regions, with the central one corresponding to the fully developed Poiseuille–Couette flow. But for these high values of A, the structure of the downwind region is more complex. At $A = 12.5$ (figure 11) a second corotating vortex appears for $Re \geqslant 6.67 \times 10^2$, the strength of which is observed to increase with Re. At $A = 25$ (figure 12) the two-cell structure again exists for $Re = 6.67 \times 10^2$, but for $Re \geqslant 1.33 \times 10^3$ a third vortex is generated in the downward region, with the onset of a fourth roll at $Re = 5 \times 10^3$.

For a better interpretation of the effect of the different parameters on this flow structure, velocity profiles across the cavity at $y = \frac{1}{2}A$ are given in figures 13 and 14 for $A = 12.5$ and $A = 25$, respectively. For small Re, i.e. $Re \leqslant 3.33 \times 10^2$ at $A = 12.5$

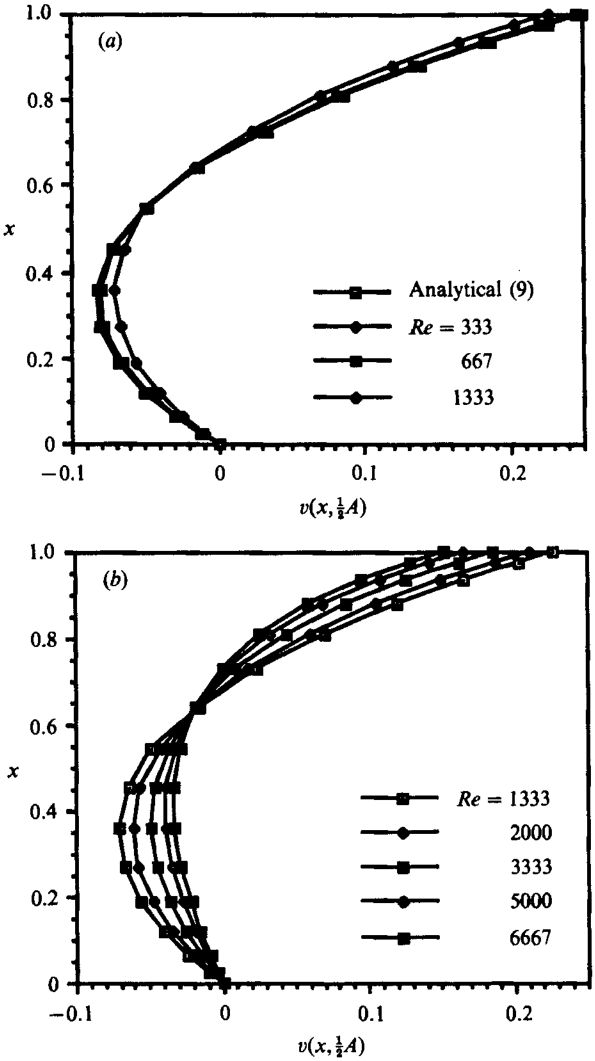

FIGURE 14. Velocity profile $v(x)$ at $y = \frac{1}{2}A$ for $A = 25$: (*a*) $Re \leqslant 1.33 \times 10^3$, (*b*) $Re \geqslant 1.33 \times 10^3$.

and $Re \leqslant 6.67 \times 10^2$ at $A = 25$, the solution is quite similar to the Poiseuille–Couette solution (9) (see figures 13*a* and 14*a*), while for higher and higher Re these velocity profiles differ increasingly from it (see figures 13*b* and 14*b*).

Correspondingly, the longitudinal evolution of the surface velocity, v_{surf}, at $x = 1$ is presented in figures 15–18 in order to show how the flow, which is subject to a constant shear stress, is accelerated along the cavity in the upwind region.

For $A = 12.5$ and for small Re (figure 15*a*) the flow is shown to be rapidly accelerated and v_{surf} is seen to asymptotically reach the value 0.25 at the mid-cavity ($y/A = 0.5$) for $Re \approx 167$, and within a shorter distance for a smaller Re. A detailed view of the downwind region ($0.8 \leqslant y/A \leqslant 1$) in figure 15(*b*) reveals that v_{surf} slightly overshoots 0.25 near the endwall for $Re > 167$. But for $Re \geqslant 2 \times 10^3$ the flow, which is still accelerated in the upwind region (figure 16*a*), slows down before reaching 0.25, when approaching the endwall (figure 16*b*); this confinement effect of the endwall increases with Re.

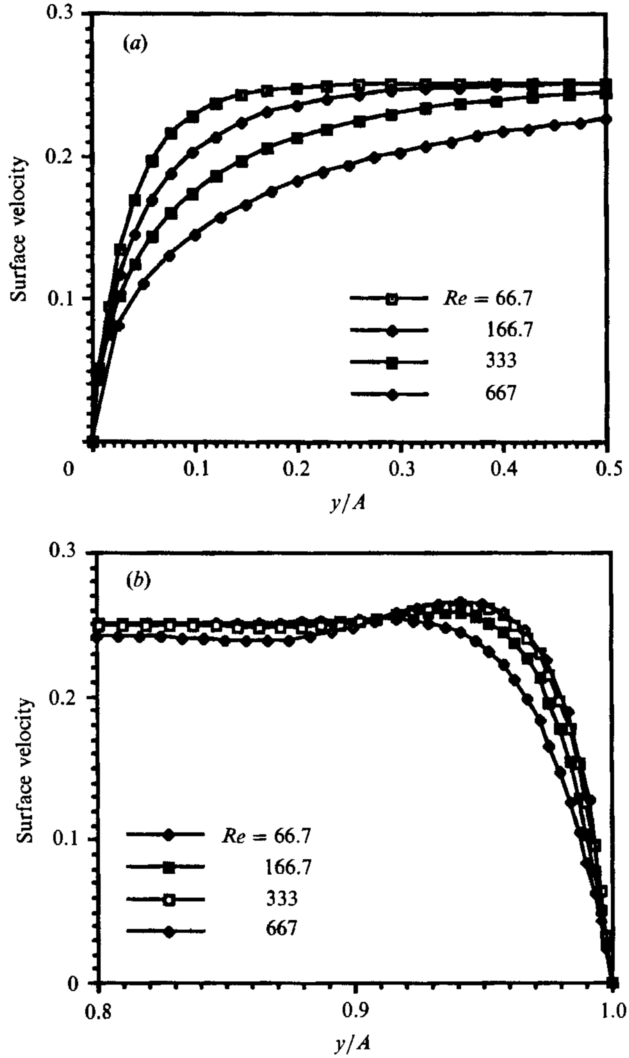

FIGURE 15. Surface velocity versus y/A at $A = 12.5$ for various $Re \leqslant 6.67 \times 10^2$; (a) $0 \leqslant y/A \leqslant 0.5$ (upwind) and (b) $0.8 \leqslant y/A \leqslant 1$ (downwind).

The same kind of behaviour of the v_{surf} curves in the upwind region is observed at $A = 25$, for values of Re about twice as large (see figures 17 and 18). This similarity suggests that the v_{surf} results can be correlated in terms of the distance y (from the upwind endwall) and of the reciprocal of Re, as for the classical entrance problem of a straight channel (Schlichting 1968). For such correlations in terms of y/Re, we eliminated the values corresponding to the end regions (in order to avoid the direct endwall effects); the results are presented in figures 19(a), 19(b) and 19(c) for $A = 4$, $A = 12.5$ and $A = 25$, respectively. This similarity in terms of y/Re can also be seen in figure 20 in which v_{surf} is plotted for the three different A, for $Re = 3.33 \times 10^2$ and $Re = 3.33 \times 10^3$. From figures 19 and 20, a development length, l_e, at which v_{surf} approaches the limiting value 0.25 to within 1%, can be evaluated. This length, based on H, corresponds approximately to

$$l_e = 0.025\, Re. \tag{11}$$

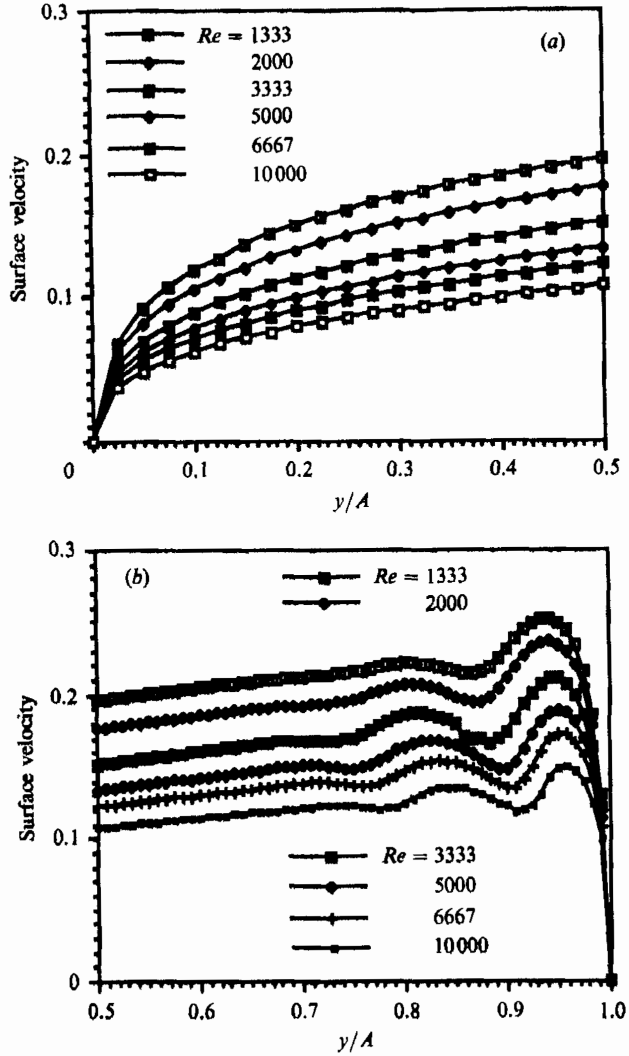

FIGURE 16. Surface versus y/A at $A = 12.5$ for various Re in the range $1.33 \times 10^3 \leqslant Re \leqslant 10^4$; (*a*) $0 \leqslant y/A \leqslant 0.5$ and (*b*) $0.5 \leqslant y/A \leqslant 1$.

It can be compared to the inlet length for a straight channel, $l_e/H = 0.04\,Re$, where Re is based on the height of the channel and the entrance velocity (Schlichting 1968). Thus we can define a condition (linking Re and A) for the observability of the fully developed Poiseuille–Couette flow at the mid-cavity, i.e. $l_e \leqslant \frac{1}{2}A$. From (11), this condition simply becomes

$$Re \leqslant 20A. \tag{12}$$

Another interesting feature is that, for a given $Re \leqslant 2 \times 10^3$, the y-position of the extrema of v_{surf} along the cavity in the downwind region appears to be almost the same for $A = 12.5$ and $A = 25$. This can be seen by comparing figures 21 (*a*) and 21 (*b*), for $Re = 1.33 \times 10^3$ and $Re = 2 \times 10^3$, respectively. For higher Re (see figures 21 (*c*) and 21 (*d*) for $Re = 3.33 \times 10^3$ and $Re = 6.67 \times 10^3$, respectively) the confinement effect becomes more and more evident. This can also be seen by comparing the (steady) flow patterns for $A = 12.5$ and $A = 25$, respectively in figures 11 and 12 (for various

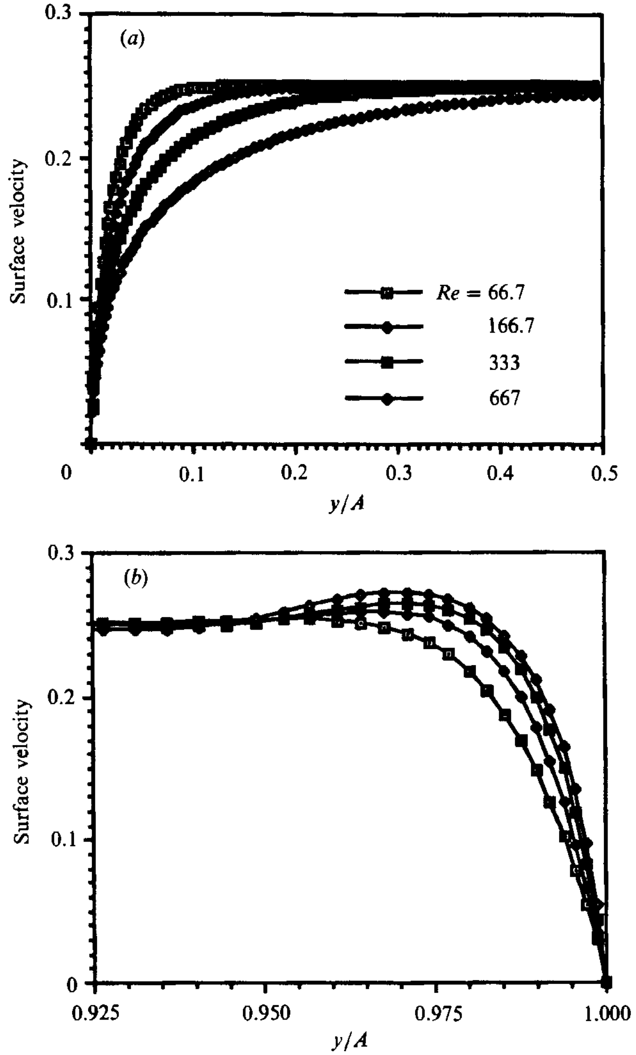

FIGURE 17. Surface velocity versus y/A at $A = 25$ for various Re in the range $6.67\times10^1 \leqslant Re \leqslant 6.67\times10^2$; (a) $0 \leqslant y/A \leqslant 0.5$ (upwind) and (b) $0.925 \leqslant y/A \leqslant 1$ (downwind).

Reynolds numbers). In particular, for $Re = 2\times10^3$ a third vortex is shown to exist at $A = 25$ (figure 12e) and not at $A = 12.5$ (figure 11e); this is attributed to a confinement (viscous damping) effect. Similarly, for $Re = 1.33\times10^4$ a fourth vortex exists at $A = 25$ (figure 12j), and not at $A = 12.5$ (figure 11j).

The computations did not show any evidence of oscillatory behaviour in the whole range of Re and A considered herein ($Re \leqslant 5\times10^4$ for $A = 4$; $Re \leqslant 2\times10^4$ for $A = 12.5$; $Re \leqslant 1.67\times10^4$ for $A = 25$). Of course this is not in contradiction with the stability results given by Smith & Davis (1983), as our model is limited to rectangular (two-dimensional) cavities with conducting horizontal boundaries, while the onset of oscillatory instabilities predicted by Smith & Davis (1983) correspond to undamped three-dimensional disturbances in the case of prescribed heat flux. (We note, in addition, that the stability theory of Smith & Davis (1983) applies only for disturbances superimposed on the fully developed Poiseuille–Couette flow, which only exists when condition (12) is satisfied.) The steady behaviour given by the

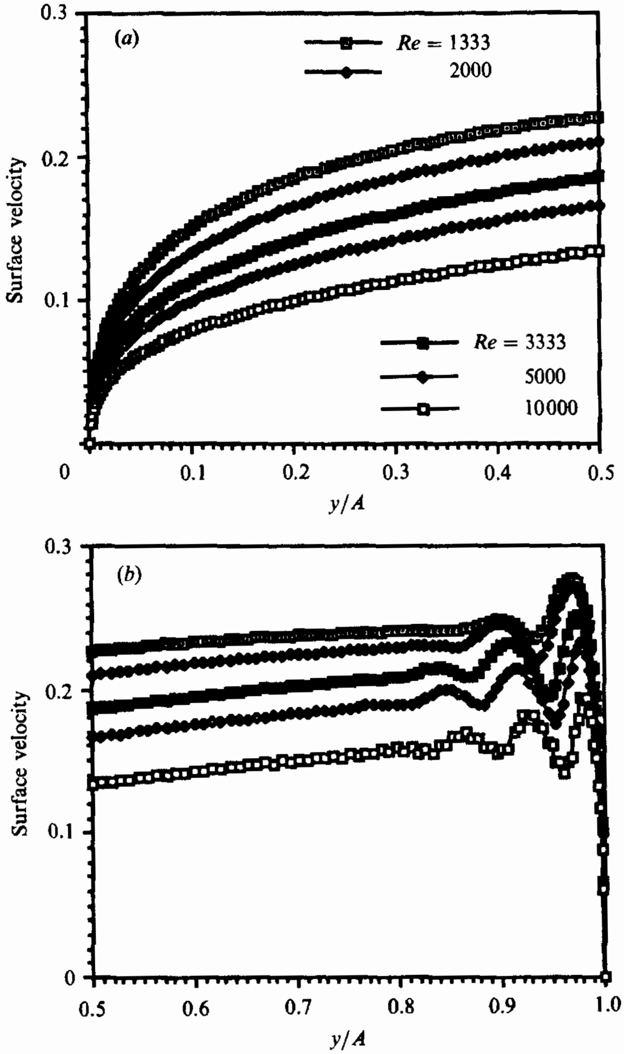

FIGURE 18. Surface velocity versus y/A at $= 25$ for various Re in the range $1.33 \times 10^3 \leqslant Re \leqslant 10^4$; (*a*) $0 \leqslant y/A \leqslant 0.5$ and (*b*) $0.5 \leqslant y/A \leqslant 1$.

calculations is in agreement with the experimental results reported by Camel *et al.* (1986) for a long cavity filled with liquid tin ($Pr = 0.015$).

Comparisons between experimental (Camel *et al.* 1986) and numerical results concerning the surface velocity have been given in a previous paper by Ben Hadid *et al.* (1988) for four aspect ratios, $A = 2$, 4, 12.5 and 25. There is good agreement between these results, especially for high values of Reynolds number where a boundary-layer regime prevails. This boundary-layer regime has been shown to occur for $Re/A > 200$, and the computed surface velocities at $y = \frac{1}{2}A$ (still non-dimensionalized by $Re\,\nu/H$), which were correlated in terms of Reynolds number and aspect ratio, exhibited the following behaviour:

$$v_{\mathrm{surf},\, y=\frac{1}{2}A} \approx a(Re/A)^{-\frac{1}{3}}, \quad \text{with } a \approx 0.95. \tag{13}$$

In fact this result can be compared, as kindly suggested by one of the referees, to the classical shear-driven boundary-layer solution (based on the balance between

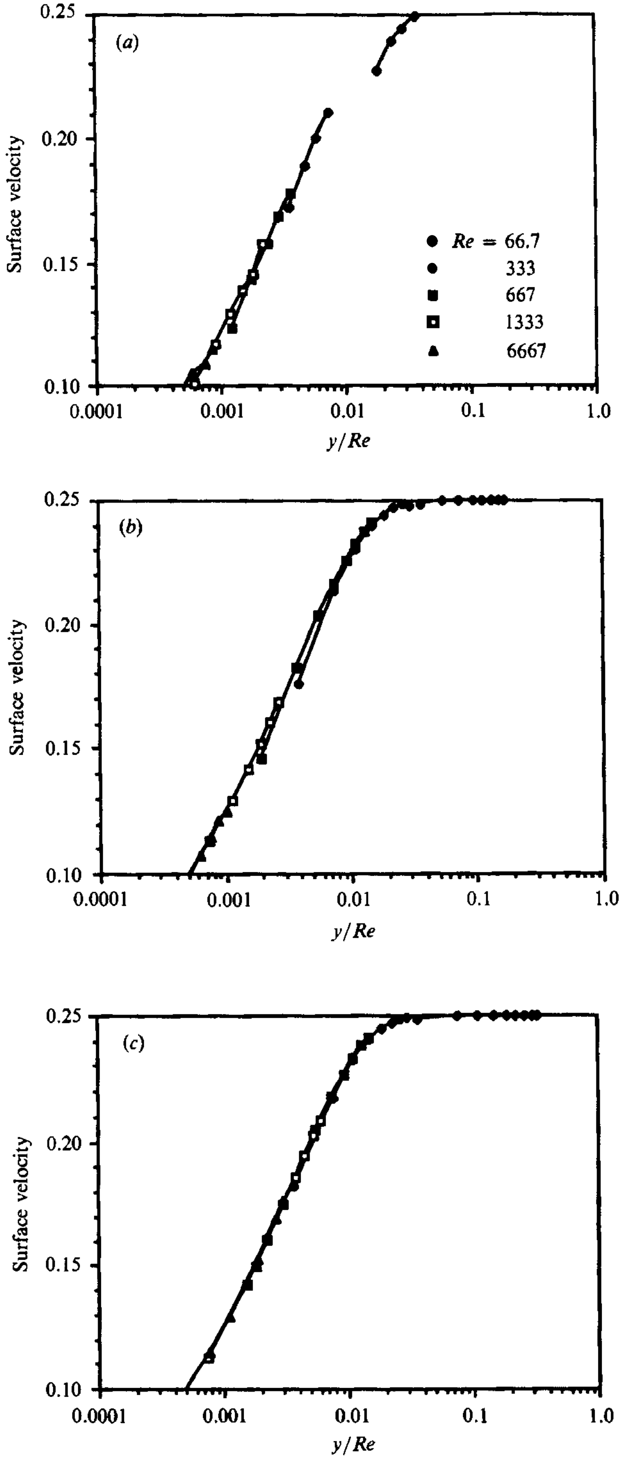

FIGURE 19. Correlation giving v_{surf} versus y/Re in the upwind region for various Re; (*a*) $A = 4$; (*b*) $A = 12.5$ and (*c*) $A = 25$.

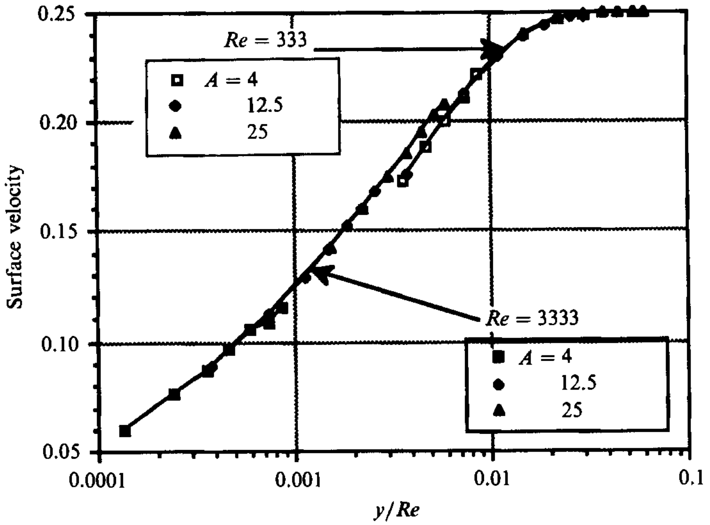

FIGURE 20. Correlation giving v_{surf} versus y/Re in the upwind region for different A, at $Re = 3.33 \times 10^2$ and $Re = 3.33 \times 10^3$.

inertia and viscous forces), which states that for a given (constant) shear stress, $S = \partial\sigma/\partial y^* = \mu \partial v^*/\partial x^*$, the flow is driven in a thin layer of thickness δ^* near the interface, such that (when using primitive variables):

$$v^* \frac{\partial v^*}{\partial y^*} \approx \nu \frac{\partial^2 v^*}{\partial x^{*2}} \quad \text{(inertia and viscous forces balance)} \tag{14}$$

and

$$\mu \frac{\partial v^*}{\partial x^*} \approx S \quad \text{(boundary condition).} \tag{15}$$

From (15), the thickness of the surface-driven flow is given by $\delta^* \propto \mu v^*/S$. Inserting this expression in (14) leads to the relation $v^{*3} \propto S^2 \nu y^*/\mu^2$, and thus

$$v^* \propto [S^2 y^*/(\rho^2 \nu)]^{\frac{1}{3}} \tag{16}$$

and

$$\delta^* \propto (y^* \rho \nu^2/S)^{\frac{1}{3}}. \tag{17}$$

Thus, using the previous non-dimensionalization, we get

$$\left.\begin{aligned} v_{\text{surf}} &\propto (y/Re)^{\frac{1}{3}}, \\ v_{\text{surf},\,y-A} &\propto (A/Re)^{\frac{1}{3}}, \end{aligned}\right\} \tag{18}$$

$$\delta = \delta^*/H \propto (y/Re)^{\frac{1}{3}}. \tag{19}$$

The computed values of v_{surf} for $Re = 3.33 \times 10^3$, $Re = 5 \times 10^3$, $Re = 6.67 \times 10^3$ and $Re = 10^4$, are given in logarithmic coordinates in terms of y/Re in figure 22. The four corresponding curves reach the slope $\frac{1}{3}$ for y/Re larger than about 2×10^{-4} at $Re = 3.33 \times 10^3$ and for even smaller y/Re at higher Re. Of course, for the lowest Re ($Re = 3.33 \times 10^3$) where fully developed Poiseuille–Couette flow can be reached, the slope decreases and vanishes for high y/Re.

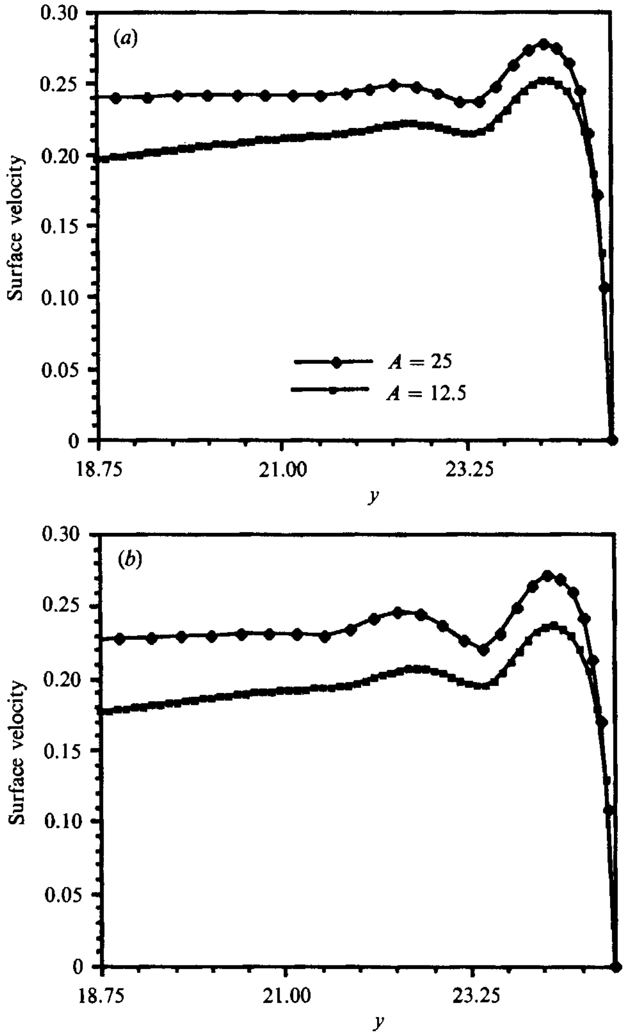

FIGURE 21 (*a*, *b*). For caption see facing page.

5. Conclusions

A numerical simulation of the flow driven by thermocapillary forces on the free surface of a long horizontal layer subjected to a horizontal temperature gradient has been carried out for different aspect ratios and a wide range of values of the Reynolds–Marangoni number, $0 \leqslant Re \leqslant 5 \times 10^4$.

In the case of low-Prandtl-number fluids ($Pr = 0.015$) considered herein, it appears that the flow field is almost independent of the temperature field. As an example, for aspect ratio $A = 4$ we have shown that the flow field and the surface velocity are essentially the same for both insulating and conducting horizontal walls. Most of the results presented concern the conducting case, for which the driving forces are constant along the free (upper) surface of the cavity. In that case the flow field is strictly independent of the thermal field inside the fluid layer (the buoyancy forces being neglected).

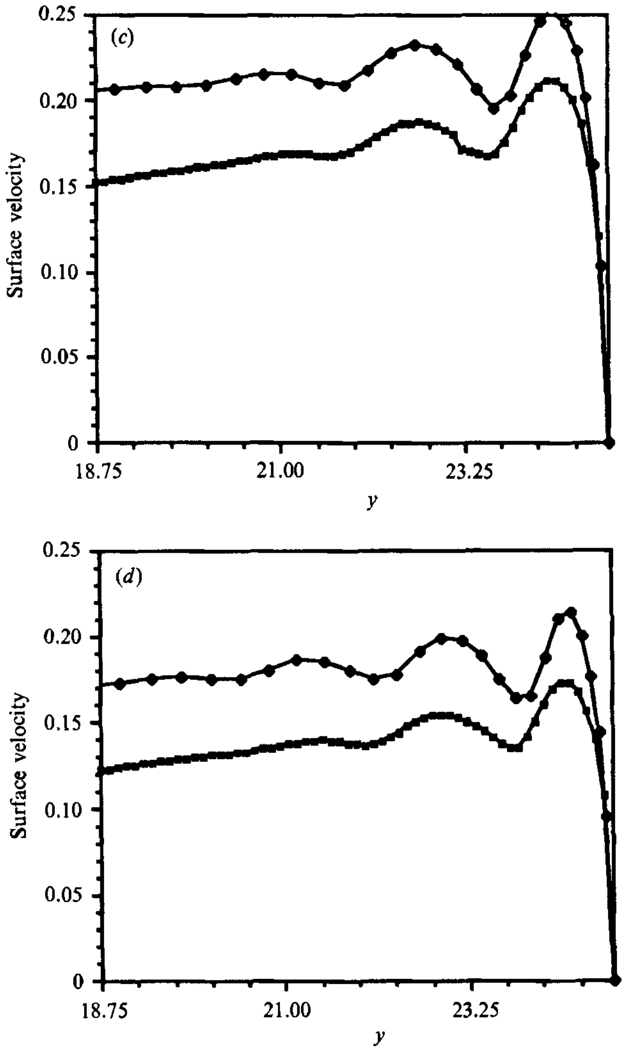

FIGURE 21. Surface velocity versus y in the downwind region for $A = 12.5$ and $A = 25$; for (*a*) $Re = 1.33 \times 10^3$; (*b*) 2×10^3; (*c*) 3.333×10^3; (*d*) 6.667×10^3.

For small Re the flow is shown to reach the fully developed Poiseuille–Couette flow solution (valid for infinitely long layers) in the central region of the cavity. In addition to this central region, two other characteristic regions have been identified: an upwind region in which the flow is accelerated to reach this Poiseuille–Couette solution, and a downwind region in which the flow is decelerated and deflected by the endwall at $y = A$. A condition for the observability of the Poiseuille–Couette flow is derived as $Re \leqslant 20A$ (condition (12)). For high Re, exceeding this value, the surface velocity is smaller than the value 0.25 corresponding to the Poiseuille–Couette solution at $x = 1$. The length of the region of fully developed Poiseuille–Couette flow is reduced and even disappears, when Re increases; this means that the upwind and downwind regions then occupy an increasing part of the cavity and finally coalesce.

The downwind region exhibits a complex structure, in particular for the high aspect ratios. When Re increases, a multi-vortex pattern is obtained in which the

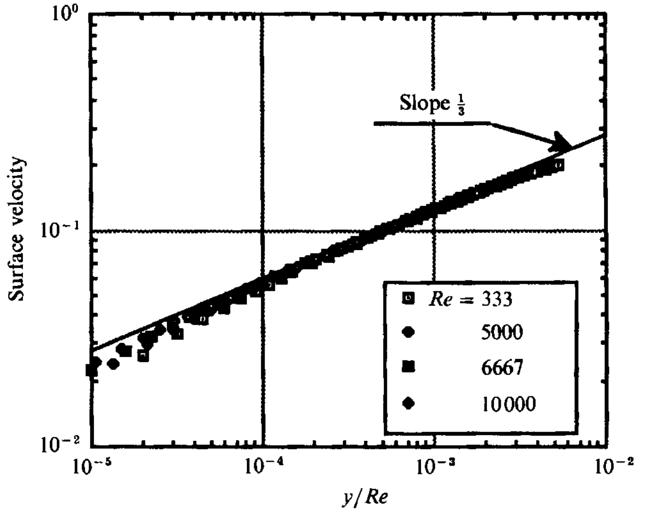

FIGURE 22. Surface velocity versus y/Re for $A = 25$, for $Re = 3.333 \times 10^3$, 5×10^3, 6.667×10^3 and 10^4.

number of vortices increases with Re. However, the number of vortices does not depend on A, as long as the condition (12) is satisfied. When this condition is not satisfied some of the vortices are suppressed.

For all the values of Re and A considered in the present study, no evidence of oscillatory behaviour has been found, in agreement with experimental results reported by Camel *et al.* (1986).

The authors gratefully acknowledge Jean Jacques Favier, Denis Camel and Pierre Tison who contributed to this study through enlightening discussions and private communications. They are grateful also to Professor Franz Rosenberger for helpful suggestions on improving the original manuscript. This research was financially supported by the Centre National d'Etudes Spatiales (Division Microgravité Fondamentale et Appliquée) and the Direction Recherches et Etudes Techniques (Groupe Hydrodynamique).

REFERENCES

AVDUYEVSKY, V. S., GRISHIN, S. D., LESKOV, L. V., POLEZHAEV, V. I. & SAVITCHEV, V. V. 1984 Scientific foundations of Space manufacturing. *Advances in Science and Technology in USSR*. MIR.

BALASUBRAMANIAN, R. & OSTRACH, S. 1984 Fluid motion in the czochralski method of crystal growth. *PhysicoChem. Hydrodyn.* **5**, 3–18.

BENGURIA, R. D. & DEPASSIER, M. C. 1989 On the linear stability theory of Bénard–Marangoni convection. *Phys. Fluids* A **1**, 1123–1127.

BEN HADID, H. 1989 Etude numérique des mouvements convectifs au sein des fluides de faible nombre de Prandtl. Application à la fabrication des matériaux. Doctorate thesis, Université d'Aix-Marseille II.

BEN HADID, H., ROUX, B., LAURE, P., TISON, P., CAMEL, D. & FAVIER, J. J. 1988 Surface-tension-driven flow in horizontal liquid metal layers. *Adv. Space Res.* **8**, 293–304.

BEN HADID, H., ROUX, B., RANDRIAMAMPIANINA, A., CRESPO, E. & BONTOUX, P. 1987 Onset of oscillatory convection in horizontal layers of low-Prandtl-number melts. In *Interfacial Phenomena* (ed. M. G. Velarde), pp. 997–1028, Plenum.

BERGMAN, T. L. & KELLER, J. R. 1988 Combined buoyancy-surface tension flow in liquid metals. *Numer. Heat Transfer* **13**, 49–63.

BERGMAN, T. L. & RAMADHYANI, S. 1986 Combined buoyancy- and thermocapillary-driven convection in open square cavities. *Numer. Heat Transfer* **9**, 441–451.

BIRIKH, R. V. 1966 Thermocapillary convection in a horizontal layer of liquid. *J. Appl. Mech. Tech. Phys.* **7**, 43.

BYE, J. A. T. 1966 Numerical solution of the steady-state vorticity equation in rectangular basins. *J. Fluid Mech.* **26**, 577–598.

CAMEL, D., TISON, P. & FAVIER, J. J. 1986 Marangoni flow regimes in liquid metals. *Acta Astron.* **13**, 723–726.

CARRUTHERS, J. R. 1977 Thermal convection instabilities relevant to crystal growth from liquids. In *Preparation and Properties of Solid State Materials*, Vol. 3 (Ed. W. R. Wilcox & R. A. Lefever), New York: M. Dekker.

CASTILLO, J. L. & VELARDE, M. G. 1982 Buoyancy–thermocapillary instability: the role of interfacial deformation in one- and two-component fluid layers heated from below or above. *J. Fluid Mech.* **125**, 463–474.

CERISIER, P., PANTALONI, J., FINIELS, G. & AMALRIC, R. 1982 Thermovision applied to Bénard–Marangoni convection. *Appl. Opt.* **21**, 2153–2159.

CHUN, CH.-H. 1980 Marangoni convection in a floating zone under reduced gravity. *J. Cryst. Growth* **48**, 600.

COWLEY, S. J. & DAVIS, S. H. 1983 Viscous thermocapillary convection at high Marangoni number. *J. Fluid Mech.* **135**, 175–188.

CUVELIER, C. 1986 On the computation of fluid boundaries. In *Notes on Numerical Fluid Mechanics*, vol. 17 (ed. P. Wesseling), pp. 18–29. Vieweg.

CUVELIER, C. & DRIESSEN, J. M. 1986 Thermocapillary free boundaries in crystal growth. *J. Fluid Mech.* **169**, 1–26.

DAVIS, S. H. 1987 Thermocapillary instabilities. *Ann. Rev. Fluid Mech.* **19**, 403–435.

FAIRWEATHER, G. & MITCHELL, A. R. 1967 A new computational procedure for A.O.I methods. *SIAM J. Numer. Anal.* **4**, 2.

FU, B.-I. & OSTRACH, S. 1983 Numerical solutions of thermocapillary flows in floating zones. In *Transport Phenomena in Materials Processing*. Natural Convection-HTD-vol. 16, pp. 91–104. ASME.

KAZARINOFF, N. D. & WILKOWSKI, J. S. 1989 A numerical study of Marangoni flows in zone-refined silicon crystals. *Phys. Fluids* A **1**, 625–627.

KIRDYASHKIN, A. G. 1984 Thermogravitional and thermocapillary flows in a horizontal liquid layer under the conditions of a horizontal temperature gradient. *Intl J. Heat Mass Transfer* **27**, 1205–1218.

LANGLOIS, W. E. 1985 Buoyancy-driven flows in crystal-growth melts. *Ann. Rev. Fluid Mech.* **17**, 191–215.

LEGROS, J. C., PETRÉ, G. & LIMBOURG-FONTAINE, M. CL. 1983 The influence on the Marangoni effect of a surface tension minimum as a function of temperature in microgravity conditions. In *Proc. 4th European Symp. Materials Sciences under Microgravity*, ESA-SP-191, pp. 201–203.

LEVICH, V. G. & KRYLOV, V. S. 1969 Surface-tension-driven phenomena. *Ann. Rev. Fluid Mech.* **1**, 293–316.

METZGER, J. & SCHWABE, D. 1988 Coupled buoyant and thermocapillary convection. *PhysicoChem. Hydrodyn.* **10**, 263–282.

NAPOLITANO, L. G. 1982 Surface and buoyancy driven free convection. *Acta Astron.* **9**, 199–215.

NAPOLITANO, L. G., GOLIA, C. & VIVIANI, A. 1984 Numerical simulation of unsteady thermal Marangoni flows. *Proc. 5th European Symp. Materials Sciences in Microgravity conditions*, ESA-SP-222, pp. 251–258.

NAPOLITANO, L. G. & MONTI, R. 1987 Surface driven flows: recent theoretical and experimental results. *Proc. 6th European Symp. Materials Sciences in Microgravity conditions*, ESA-SP-256, pp. 551–555.

NEARY, M. D. & STEPHANOFF, K. D. 1987 Shear-layer-driven transition in a rectangular cavity. *Phys. Fluids* **30**, 2936–2946.

NIELD, D. A. 1964 Surface tension and buoyancy effects in cellular convection. *J. Fluid Mech.* **19**, 341–352.

OCHIAI, J., KUWAHARA, K., MORIOKA, M., ENYA, S., SEZAKI, K., MAEKAWA, T. & TANASAWA, I. 1984 Experimental study on Marangoni convection. *Proc. 5th European Symp. Materials Sciences in Microgravity conditions*, ESA-SP-222, pp. 291–295.

OSTRACH, S. 1976 Convection Phenomena at reduced gravity of importance for materials processing. *Proc. Second European Symp. Material Sciences in Space*, ESA-SP-114, pp. 41–56.

OSTRACH, S. 1982 Low-gravity fluid flows. *Ann. Rev. Fluid Mech.* **14**, 313–345.

PEARSON, J. R. A. 1958 On convection cells induced by surface tension. *J. Fluid Mech.* **4**, 489–500.

PIMPUTKAR, S. M. & OSTRACH, S. 1981 Convective effects in crystals grown from melts. *J. Cryst. Growth* **55**, 614–646.

PLATTEN J. K. & LEGROS, J. C. 1986 *Convection in Liquids*, pp. 407–412. Springer.

POLEZHAEV, V. I. 1984 *Hydrodynamics, Heat and Mass Transfer During Crystal Growth*. Springer.

POLEZHAEV, V. I., DUBOVIK, K. G., NIKITIN, S. A., PROSTOMOLOTOV, A. I. & FEDYUSHKIN, A. I. 1981 Convection during crystal growth on Earth and in Space. *J. Cryst. Growth* **52**, 465–470.

PREISSER, F., SCHWABE, D. & SCHARMANN, A. 1983 Steady and oscillatory thermocapillary convection in liquid columns with free cylindrical surface. *J. Fluid Mech.* **126**, 545–567.

ROSENBERGER, F. 1979 *Fundamentals of Crystal Growth*, pp. 387–391. Springer.

ROUX, B., BONTOUX, P., LOC, T. P. & DAUBE, O. 1979 Optimisation of Hermitian methods for N.S. equations in vorticity and streamfunction formulation. Lecture Notes in Mathematics, vol. 771, pp. 450–468. Springer.

ROUX, B., GRONDIN, J. C., BONTOUX, P. & GILLY, B. 1978 On a high-order accurate method for the numerical study of natural convection in a vertical square cavity. *Numerical Heat Transfer* **1**, 331–349.

SCHLICHTING, H. 1968 *Boundary Layer Theory* (6th edn), pp. 176–178. McGraw-Hill.

SCHWABE, D. & SCHARMANN, A. 1981 The magnitude of thermocapillary convection in larger melt volumes. *Adv. Space Res.* **1**, 13–16.

SCHWABE, D. & SCHARMANN, A. 1988 Marangoni and Buoyant convection in an open cavity under reduced and normal gravity. *XXVII COSPAR*, G.1.3.1, Helsinki.

SCRIVEN, L. E. & STERNLING, C. V. 1964 On cellular convection driven by surface tension gradients: effects of mean surface tension and surface viscosity. *J. Fluid Mech.* **9**, 321–340.

SEN, A. K. & DAVIS, S. H. 1982 Steady thermocapillary flows in two-dimensional slots. *J. Fluid Mech.* **121**, 163–186.

SMITH, K. A. 1966 On convective instability induced by surface-tension gradient. *J. Fluid Mech.* **24**, 401–414.

SMITH, M. K. 1988 The nonlinear stability of dynamic thermocapillary liquid layer. *J. Fluid Mech.* **194**, 391–415.

SMITH, M. K. & DAVIS, S. H. 1983 Instabilities of dynamic thermocapillary liquid layers. Part 1 Convective instabilities. *J. Fluid Mech.* **132**, 119–144.

SRINIVASAN, J. & BASU, B. 1986 A numerical study of thermocapillary flow in a rectangular cavity during laser melting. *Intl J. Heat Mass Transfer* **29**, 563–572.

STRANI, M. & PIVA, R. 1982 Surface tension driven flows in micro-gravity conditions. *Intl J. Numer. Meth. Fluids* **2**, 367–386.

STRANI, M., PIVA, R. & GRAZIANI, G. 1983 Thermocapillary convection in a rectangular cavity: asymptotic theory and numerical simulation. *J. Fluid Mech.* **130**, 347–376.

VAHL DAVIS, G. DE 1986 *Heat Transfer*, pp. 101–109. Hemisphere.

VELARDE, M. G., GARCIA-YBARRA, P. L. & CASTILLO, J. L. 1987 Interfacial oscillations in Bénard–Marangoni layers. *PhysicoChem. Hydrodyn.* **9**, 387–392.

VILLERS, D. & PLATTEN, J. K. 1987 Separation of Marangoni convection from gravitational convection in earth experiments. *PhysicoChem. Hydrodyn.* **9**, 173–183.

VILLERS, D. & PLATTEN, J. K. 1989 Influence of thermocapillarity on the oscillatory convection in low-*Pr* fluids. In *Notes in Numerical Fluid Mechanics*, vol. 27, pp. 108–116. Vieweg.

WILKE, H. & LÖSER, W. 1983 Numerical calculation of Marangoni convection in a rectangular open boat. *Cryst. Res. Tech.* **18**, 825–833.

WINTERS, K. H., PLESSER, TH. & CLIFFE, K. A. 1988 The onset of convection in a finite container due to surface tension and buoyancy. *Physica* D **29**, 387–401.

XU, J. J. & DAVIS, S. H. 1984 Convective thermocapillary instability in liquid bridges. *Phys. Fluids* **27**, 1102–1107.

YIH, C.S. 1968 Fluid motion induced by surface-tension variation. *Phys. Fluids* **11**, 477–480.

ZEBIB, A., HOMSY, G. N. & MEIBURG, E. 1985 High Marangoni convection in a square cavity. *Phys. Fluids* **28**, 3467–3476.